01 Aug 2022

Self-Intercalation Tunable Interlayer Exchange Coupling in a Synthetic Van Der Waals Antiferromagnet

Xiaoqian Zhang

Wenqing Liu

Wei Niu

Qiangsheng Lu

et. al. For a complete list of authors, see https://scholarsmine.mst.edu/phys_facwork/2236

Recommended Citation

X. Zhang and W. Liu and W. Niu and Q. Lu and W. Wang and A. Sarikhani and X. Wu and C. Zhu and J. Sun and M. Vaninger and P. F. Miceli and J. Li and D. J. Singh and Y. S. Hor, "Self-Intercalation Tunable Interlayer Exchange Coupling in a Synthetic Van Der Waals Antiferromagnet," *Advanced Functional Materials*, vol. 32, no. 32, article no. 2202977, Wiley; Wiley-VCH Verlag, Aug 2022.
The definitive version is available at https://doi.org/10.1002/adfm.202202977

optical contact angle measurements and drop contour analysis to determine surface energy as well as interfacial and surface tension

force tensiometry, dynamic contact angle measurements, and force of adhesion evaluation

optical turbidity, stability and aging analysis of multi-phase dispersions

zeta potential measurements of fibres, powders, and plate-shaped solids

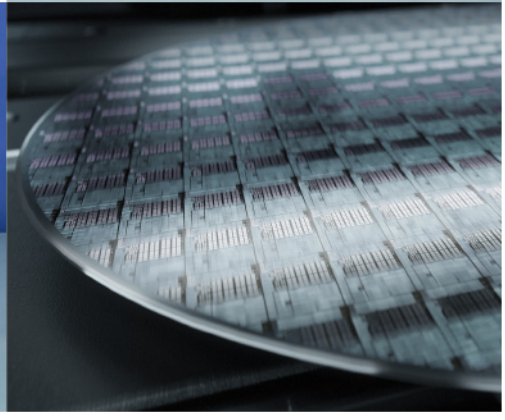

High-end, versatile laboratory measurement device portfolio for a comprehensive analysis of surfaces and interfaces

Learn more >

dataphysics
Understanding Interfaces

DataPhysics Instruments GmbH
Raiffeisenstraße 34 • 70794 Filderstadt, Germany
phone +49 (0)711 770556-0 • fax +49 (0)711 770556-99
sales@dataphysics-instruments.com
www.dataphysics-instruments.com

ADVANCED FUNCTIONAL MATERIALS
www.afm-journal.de

Self-Intercalation Tunable Interlayer Exchange Coupling in a Synthetic van der Waals Antiferromagnet

Xiaoqian Zhang, Wenqing Liu, Wei Niu, Qiangsheng Lu, Wei Wang, Ali Sarikhani, Xiaohua Wu, Chunhui Zhu, Jiabao Sun, Mitchel Vaninger, Paul. F. Miceli, Jianqi Li, David J. Singh, Yew San Hor, Yue Zhao, Chang Liu, Liang He, Rong Zhang,* Guang Bian,* Dapeng Yu, and Yongbing Xu**

One of the most promising avenues in 2D materials research is the synthesis of antiferromagnets employing 2D van der Waals (vdW) magnets. However, it has proven challenging, due in part to the complicated fabrication process and undesired adsorbates as well as the significantly deteriorated ferromagnetism at atomic layers. Here, the engineering of the antiferromagnetic (AFM) interlayer exchange coupling between atomically thin yet ferromagnetic $CrTe_2$ layers in an ultra-high vacuum-free 2D magnetic crystal, Cr_5Te_8 is reported. By self-introducing interstitial Cr atoms in the vdW gaps, the emergent AFM ordering and the resultant giant magnetoresistance effect are induced. A large negative magnetoresistance (10%) with a plateau-like feature is revealed, which is consistent with the AFM interlayer coupling between the adjacent $CrTe_2$ main layers in a temperature window of 30 K below the Néel temperature. Notably, the AFM state has a relatively weak interlayer exchange coupling, allowing a switching between the interlayer AFM and ferromagnetic states at moderate magnetic fields. This work represents a new route to engineering low-power devices that underpin the emerging spintronic technologies, and an ideal laboratory to study 2D magnetism.

1. Introduction

The development of engineered multilayers composed of magnetic and nonmagnetic materials at nanoscale paved the way for the creation of more complicated devices.[1,2] By stacking such thin films in multilayers, one can create layered heterostructures with properties that are fundamentally distinct from those of the constitutive bulk materials. For instance, these multilayers enable the spin valves and magnetic tunnel junctions to perform high-density and nonvolatile memories.[3,4] To realize spin-polarized scattering/tunneling, one has to create an opportunity to reorient the spin of two successive ferromagnetic (FM) layers and achieve the antiferromagnetic (AFM) interlayer coupling, which is well explained with the Ruderman–Kittel–Kasuya–Yosida (RKKY) model.[5] In this model, localized spins

X. Q. Zhang, W. Q. Liu, L. He, R. Zhang, Y. B. Xu
Jiangsu Provincial Key Laboratory of Advanced Photonic and Electronic Materials
School of Electronic Science and Engineering
Nanjing University
Nanjing 210093, China
E-mail: heliang@nju.edu.cn; rzhang@nju.edu.cn; ybxu@nju.edu.cn

X. Q. Zhang, Y. Zhao, C. Liu, D. P. Yu
Shenzhen Institute for Quantum Science and Engineering
Southern University of Science and Technology
Shenzhen 518055, China

W. Q. Liu, J. B. Sun
Department of Electronic Engineering
Royal Holloway University of London
Egham, Surrey TW20 0EX, UK

W. Niu
New Energy Technology Engineering Laboratory of Jiangsu Provence & School of Science
Nanjing University of Posts and Telecommunications
Nanjing 210023, China

The ORCID identification number(s) for the author(s) of this article can be found under https://doi.org/10.1002/adfm.202202977.

DOI: 10.1002/adfm.202202977

Q. S. Lu, M. Vaninger, P. F. Miceli, D. J. Singh, G. Bian
Department of Physics and Astronomy
University of Missouri
Columbia, MO 65211, USA
E-mail: biang@missouri.edu

W. Wang
Key Laboratory of Flexible Electronics & Institute of Advanced Materials
Jiangsu National Synergetic Innovation Center for Advanced Materials
Nanjing Tech University
Nanjing 211816, China

A. Sarikhani, Y. S. Hor
Department of Physics
Missouri University of Science and Technology
Missouri 65409, USA

X. H. Wu, Y. Zhao, C. Liu
Department of Physics
Southern University of Science and Technology
Shenzhen 518055, China

C. H. Zhu, J. Q. Li
Beijing National Laboratory of Condensed Matter Physics
Institute of Physics
Chinese Academy of Sciences
Beijing 100190, China

in two FM layers interact with conduction electrons through contact exchange potential, which oscillates with the distance between them. The magnetic coupling between adjacent magnetic layers, determined by the exchange potential, therefore can be tuned by varying the thickness of the nonmagnetic spacer layers.[6,7]

Due to the mechanism of AFM interlayer coupling between adjacent FM layers, memory device designs based directly on antiferromagnets have been demonstrated. Antiferromagnets offer the benefit of being insensitive to disruptive magnetic fields while emitting no stray fields as compared to ferromagnets. In contrast to bulk antiferromagnets with large exchange fields, synthetic antiferromagnets contain a relatively low interlayer exchange coupling strength, making them ideal for studying field-induced magnetic switching.[8] At present, synthetic antiferromagnets made of transition metals have been achieved, nevertheless, the magnetic switching in synthetic antiferromagnets with van der Waals (vdW) multilayers has only been seen on rare occasions.[4,9] For this purpose, the ferromagnetism of FM layers must be maintained at atomic scale thickness.

Rich varieties of magnetic and electronic properties of 2D vdW magnets offer new options in memory computing technologies, owing to the pronounced perpendicular magnetic anisotropy (PMA) and long-range magnetic order in their ultrathin limits.[10–12] Strong covalent bonds provide an in-plane stability of 2D magnets, whereas vdW forces and the resultant relatively weak coupling enable the interlayer spin re-orientations. One example is the 2D magnetic semiconductor chromium tribromide ($CrBr_3$) with different types of stacking orders, enabling realization of either AFM or FM phases.[13] Isostructural with $CrBr_3$, CrI_3-based spin-filter magnetic tunnel junctions demonstrate an extremely large magnetoresistance (MR), with the benefit of intrinsic AFM interlayer coupling.[4] Meanwhile, antisymmetric MR has been observed in Fe_3GeTe_2/graphite/Fe_3GeTe_2 vdW heterostructures, resulting from the spin momentum locking at the interface.[14] Utilizing the vdW gap as the spacer layer, spin valves have been realized in Fe_3GeTe_2 homojunctions with a relatively low giant magnetoresistance (GMR) ratio,[15] which could be originated from the interfacial contamination during the device fabrication. In spite of the exciting progress in vdW heterostructure devices, the limitation of complicated fabrication process and interface damages occur inevitably, and the intrinsic tuning of magnetic interlayer coupling in vdW magnets remains elusive.

To achieve the AFM interlayer exchange coupling in vdW multilayers, a promising candidate is the self-intercalated 2D magnet or quasi-2D magnet, Cr_5Te_8. The Cr_5Te_8 single crystals can be regarded as a stack of alternating $CrTe_2$ and Cr intercalated layers, as shown in **Figure 1**a. Within the FM host layer, $CrTe_2$ is composed of Te–Cr–Te sandwich layers stacking along *c*-axis, and Cr atoms are covalently bonded by six nearest-neighboring Te atoms with octahedral coordination. By intercalating Cr atoms into the vdW gap, the $CrTe_2$–Cr–$CrTe_2$ stacking is formed, which is supposed to alter the FM exchange coupling of the $CrTe_2$–$CrTe_2$. Tuning of magnetic interlayer coupling in 2D vdW magnets has so far only been observed by the exfoliation of atomic layers, the electrostatic doping, as well as the substitution of atoms on chromium trihalides with a relatively low Curie temperature (T_C).[10,16,17] Recently, room-temperature ferromagnetism has been demonstrated in 2D ferromagnet $CrTe_2$ in the form of both bulk and exfoliated thin flakes.[18] Notably, the FM ordering is well preserved in $CrTe_2$ epitaxial thin films with thickness down to monolayer.[19] By means of the self-doping, Cr_5Te_8 has been reported as a weak itinerant ferromagnet with a strong PMA.[20,21] Moreover, its T_C can be well manipulated by intercalating more Cr atoms due to the competition of AFM and FM coupling.[22] In this work, we demonstrate the engineering of an AFM phase associated with AFM interlayer exchange coupling in the Cr_5Te_8 vdW magnetic crystal, which functions as a self-assembled quasi-2D spin valve.

2. Results and Discussion

Self-intercalated Cr_5Te_8 single crystals were synthesized using self-flux method (see Experimental Section). As exhibited in Figure 1a, cross-sectional scanning transmission electron microscopy (STEM) high-angle annular dark-field (HAADF) images indicate the layered trigonal crystal structure.[23] The quasi-2D layered feature is also verified by atomic force microscopy characterization on exfoliated few-layer Cr_5Te_8 flakes (Figure S1, Supporting Information). The microscopic topography taken from the surface of few-layer Cr_5Te_8 flakes shows atomically flat terraces, demonstrating the layered structure of Cr_5Te_8. The high degree of crystallinity of Cr_5Te_8 is confirmed by the selected area electron diffraction (SAED) pattern (Figure S2, Supporting Information), which could be indexed according to a trigonal crystal structure with lattice parameters of $a = 7.92$ Å, and $c = 5.98$ Å. The reduced *c* of Cr_5Te_8 relative to that of non-intercalated $CrTe_2$ (6.10 Å) suggests an increase of the coupling along *c* direction, and the significant bonding of the intercalated atoms as well. Thus, it is rather interesting to investigate the interlayer magnetic coupling, as the *c*-axis lattice constant is reduced by ≈2% after inserting Cr atoms between adjacent $CrTe_2$ layers.

Parental $CrTe_2$ has a 2D character, where vdW-type interlayer exchange coupling stabilizes a FM ground state.[24] The excess Cr atoms sit interstitially between $CrTe_2$ host layers and serve multiple functions, specifically, donating charge to the main layers to create new electronic order and modifying the bonding of the compound as well as the interlayer exchange coupling. To verify the local electronic correlation and magnetic ground state of Cr_5Te_8,[25,26] a typical pair of X-ray absorption spectroscopy (XAS) and X-ray magnetic circular dichroism (XMCD) spectra at Cr $L_{2,3}$ edge was obtained at 5 K under a magnetic field of 2 T (Figure 1b). XAS exhibits remarkable multiple-peak features, which are separated by 1.3 eV at spin–orbit core levels. The spectral line shape resembles that of pure $CrTe_2$ thin layers,[19] suggesting that Cr^{3+} cations predominate in Cr_5Te_8. The sizable XMCD spectrum, obtained by taking the

Y. B. Xu
York-Nanjing Joint Centre (YNJC) for Spintronics and Nano Engineering
Department of Electronic Engineering
The University of York
York YO10 3DD, UK

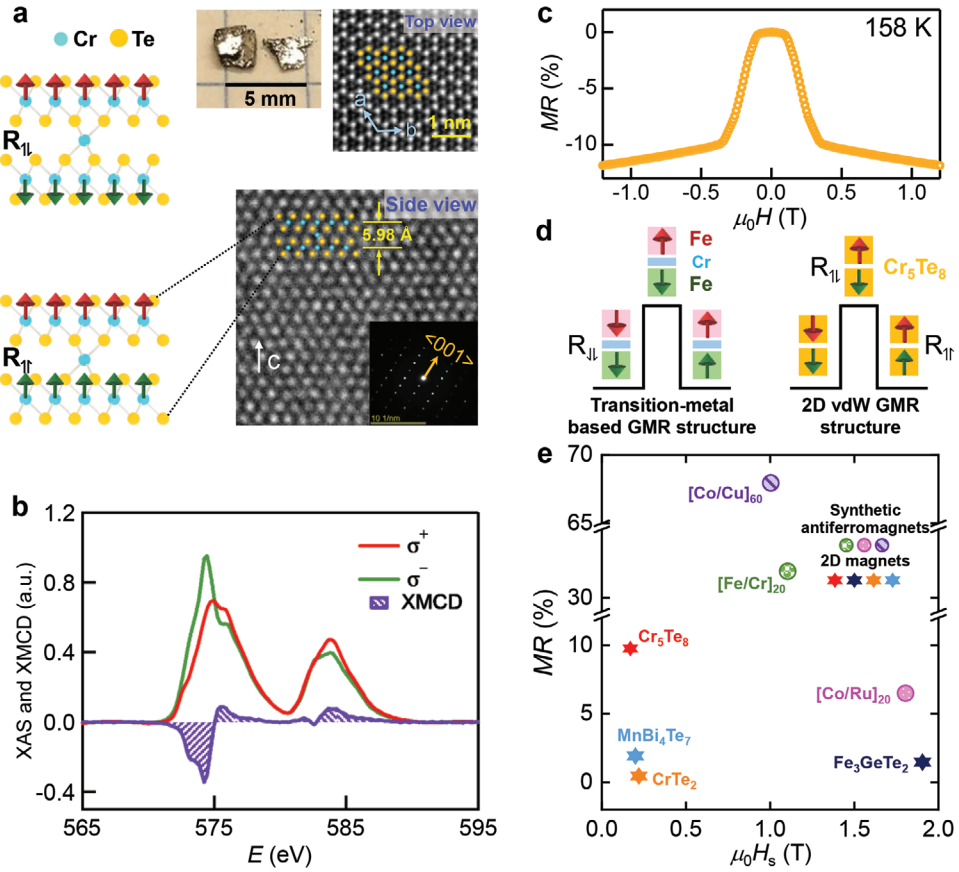

Figure 1. Crystal structure, magnetic structure, and MR of Cr_5Te_8. a) Crystal structure showing bilayer $CrTe_2$ with Cr atoms intercalated between the vdW gap. Spheres represent Te (yellow) and Cr (cyan) atoms with arrows representing interlayer magnetic exchange couplings. HAADF images from top view and side view show a trigonal lattice structure. Top panel: photo of Cr_5Te_8 single crystals. b) A typical pair of XAS for opposite circular polarizations and XMCD spectrum obtained with a magnetic field of 2 T at 5 K. c) MR curve as a function of magnetic field at 158 K. d) Schematic illustration of the transition-metal based GMR structure and the 2D vdW GMR structure. e) Plot of the MR ratio versus the saturation magnetic field (H_s), covering classic synthetic antiferromagnets ([Co/Cu]$_{60}$ (ref. [30]), [Fe/Cr]$_{20}$ (ref. [7]), [Co/Ru]$_{20}$ (ref. [7])) and 2D magnets ($MnBi_4Te_7$ (ref. [31]), Fe_3GeTe_2 (ref. [32]), $CrTe_2$ (ref. [23]), Cr_5Te_8 (this work)).

difference of XAS, manifests the intrinsic FM ground state. There is a good agreement between Cr_5Te_8 and $CrTe_2$ in both XAS and XMCD spectral line shapes, indicating that the ferromagnetism of Cr_5Te_8 mainly originate from $CrTe_2$ main layers. Furthermore, effects of self-intercalation on the magneto-transport properties were investigated (Figure 1c). Remarkably, a plateau-like feature and a large negative MR with magnitude exceeding ≈10% (0.5 T) at 158 K are observed, suggesting a distinct spin configuration in this plateau region. The high- and low-MR state could be interpreted in a manner qualitatively similar to the case of the "turn off" and "turn on" state, respectively, in a standard GMR spin valve device. Considering the low resistance along both in-plane and out-of-plane direction (Figure S3, Supporting Information), the possibility of a tunnel magnetoresistance effect could be ruled out.[4] When sweeping magnetic field, magnetization directions of the adjacent $CrTe_2$ host layers can have either a parallel or antiparallel alignment configuration due to the existence of the intercalated layers, providing evidence of the GMR effect and the resultant spin valve in Cr_5Te_8. Figure 1d presents schematics of the transition-metal based GMR structure and 2D vdW GMR structure, where the antiparallel and parallel spin alignment give rise to high ($R_{⇊}$) and low ($R_{⇈}$) resistance, respectively. In the case of conventional synthetic GMR devices composed of transition metals and alloys, electrons travel through the entire ferromagnet/metal multilayer structures, and both bulk and interfacial spin scattering are involved.[27–29] In contrast, due to the fact that the thickness of the Cr_5Te_8 GMR structure (millimeters) is much larger than the electron mean free path (tens of nanometers), the electrons are not able to pass through the entire structure to experience bulk spin scattering. Thus, the spin scattering only occurs at the interface between $CrTe_2$ main layers and the vdW gap, which could be viewed as current channels and the spacer layer, respectively. By satisfying the condition of mean free path larger than the thickness of the spacer layer combined with adjacent $CrTe_2$ layers, electrons are able to travel through both $CrTe_2$ layers and the space layer to experience interfacial spin scattering. For comparison, we made a plot of the MR ratio versus the magnetic field for classic synthetic antiferromagnets and 2D magnets (Figure 1e). The Cr_5Te_8 single crystal, as a synthetic vdW antiferromagnet, possesses a comparable MR ratio with that of conventional synthetic antiferromagnet such

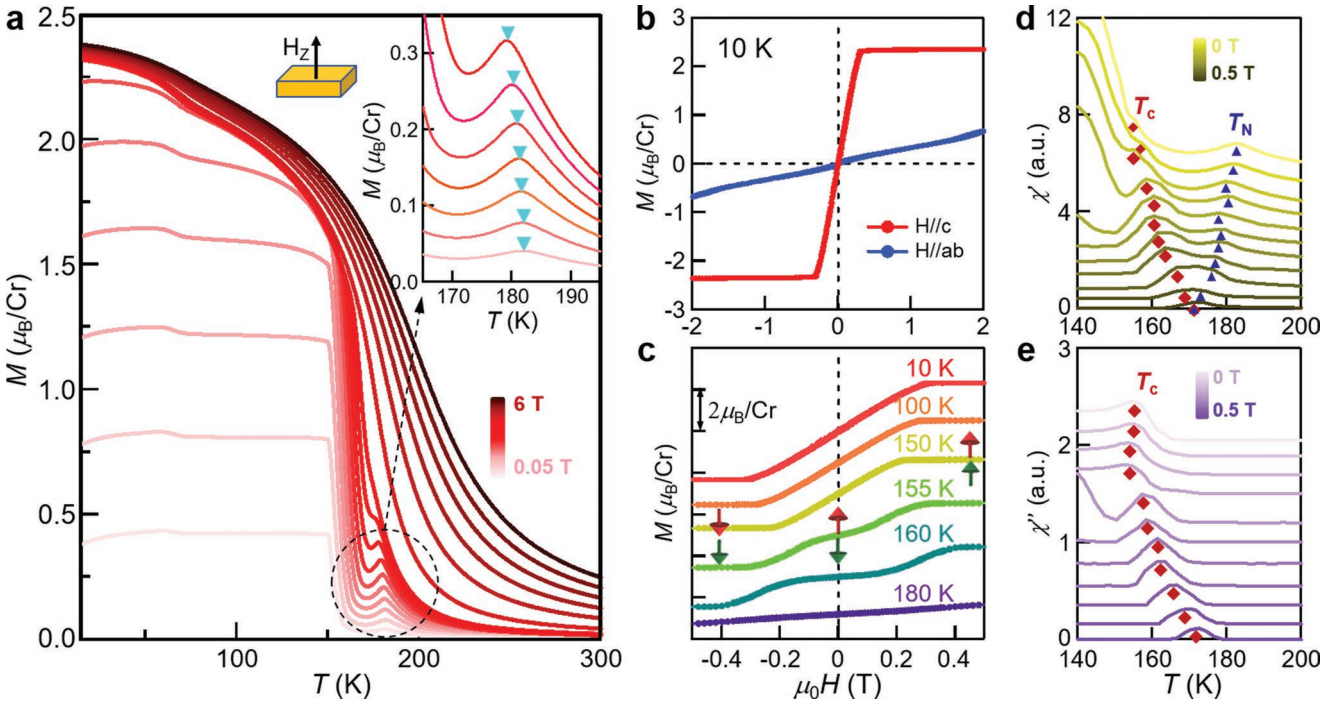

Figure 2. Demonstration of emergent AFM phase. a) Temperature dependence of the out-of-plane magnetic moment with the magnetic field ranging from 0.05 to 6 T. Samples were cooled down to 15 K without magnetic field and data was collected in the warming-up cycle. The platform-like feature and Curie-like behavior indicate that the 2D FM ordering within layers develops first. Besides, cusp-like features near 180 K (top inset) suggest development of the AFM ordering. b) Out-of-plane and in-plane magnetic hysteresis loops at 10 K, suggesting a strong PMA. c) Hysteresis loops at indicated temperatures with magnetic field along *c*-axis. The magnetization switching behavior at representative magnetic fields are schematically shown as insets. d,e) Temperature-dependent χ' and χ'' of AC susceptibility measured along out-of-plane direction. Phase boundaries of T_C and T_N determined from the susceptibility are illustrated by red squares and blue triangles.

as $[Co/Cu]_{60}$,[30] $[Co/Ru]_{20}$, and $[Fe/Cr]_{20}$,[7] but requires a lower saturation magnetic field. In addition, among 2D magnets including $MnBi_4Te_7$,[31] Fe_3GeTe_2,[32] and $CrTe_2$,[23] Cr_5Te_8 shows a pronounced intrinsic GMR ratio as observed in this work.

The emergent antiparallel spin configuration in self-intercalated Cr_5Te_8 indicates the existence of extra magnetic states, apart from the FM phase in $CrTe_2$.[18] The magnetic order was revealed by monitoring the temperature and field dependent magnetization. **Figure 2**a shows the temperature dependent magnetization (M–T) curves with an applied magnetic field perpendicular to the sample surface. The magnetization shows a general trend of decreasing with the increase of temperature, demonstrating a FM behavior with a T_C of ≈150 K. Above T_C, a cusp-like feature is observed in the M–T curve, exhibiting a typical AFM property with a Néel temperature (T_N) of 180 K. As the magnetic field increases, T_N shifts to lower temperature, and disappears when the field exceeds 0.5 T (inset of Figure 2a). In addition to M–T curves, the magnetic hysteresis loops also indicate the FM nature when the temperature is below T_C. As shown in Figure 2b, the out-of-plane magnetic moment increases linearly and saturates at a relatively low magnetic field (below 0.3 T). The saturated magnetic moment (M_s) per Cr atom and coercive field is determined to be 2.3 μ_B and 0.01 T at 10 K, respectively. An itinerant nature appears to be the reason of the discrepancy from the M_s = 3 μ_B expected under an ionic model. In contrast, the in-plane magnetization does not saturate even with a strong magnetic field of 5 T (Figure S7, Supporting Information). This demonstrates a strong PMA, which is related to the strong overlap of Cr–Cr $3d_{z^2}$ and Cr 3*d*–Te 5*p*-orbitals along the perpendicular direction. Remarkably, when the temperature is above T_C, a plateau feature appears in the hysteresis loops at low field region (Figure 2c), indicative of an AFM coupling with almost vanishing magnetic moment. This plateau feature is also a signature of magnetic anisotropy, echoing the PMA discussed above. Further increasing the field, the AFM order is suppressed, and a spin-flip transition occurs. The AFM phase is preserved at a higher field with elevated temperature, and disappears with temperature above T_N. Because of the weak quasi-vdW interlayer exchange coupling, the magnetic properties can be easily modified by applying a low magnetic field or varying the temperature. To further investigate the magnetic states, we measured the temperature-dependent AC susceptibility under different out-of-plane fields. The real part (χ') and imaginary part (χ'') of magnetic susceptibility under magnetic field ranging from 0 to 0.5 T with a step of 0.05 T are presented in Figure 2d,e, respectively. χ' exhibits an extra peak (marked by blue triangles) beside the FM peak (red squares), while only a FM peak shows up in χ'' within the identical temperature scope. The prominent χ' and absent χ'' of the anomaly in the magnetization curve is another evidence of an AFM character.

The intriguing AFM ordering makes Cr_5Te_8 promising for engineering spin valve devices. Accordingly, electrical properties under magnetic field along the easy axis at various

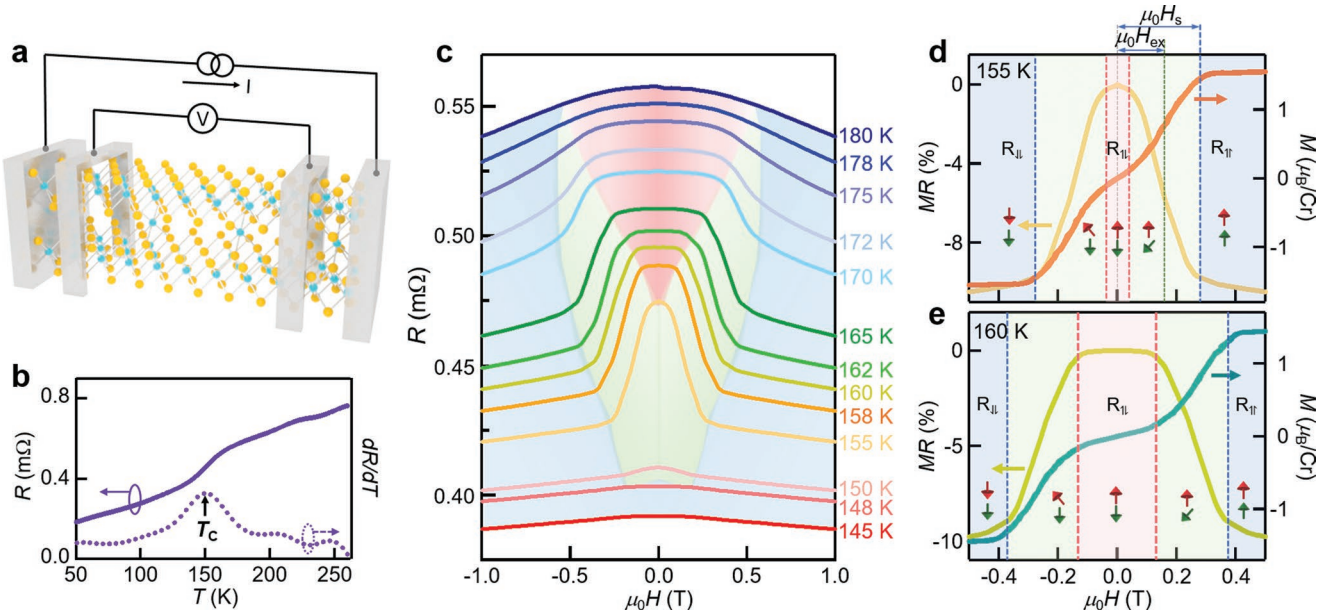

Figure 3. AFM interlayer exchange coupling in Cr_5Te_8 spin valves. a) Schematic diagram of transport measurements. b) Temperature dependent longitudinal resistance and its differential, dR/dT, exhibiting a kink at T_C ≈150 K. c) Longitudinal resistance versus out-of-plane magnetic field. There is a rapid increasement of MR once entering into the AFM state. With further increasing temperature, the MR decreases and vanishes above T_N. d) Comparison of field dependent MR (yellow line) and magnetic moment M (orange line) at 155 K, demonstrating the slope change at higher field due to the saturated magnetization. The MR ratio is defined as $[\rho(H)-\rho(0)]/\rho(0)$. e) Slope change of field dependent MR (light green line) and magnetic moment M (green line) at 160 K, suggesting a phase transition.

temperatures were assessed systematically (**Figure 3**a). The temperature dependent longitudinal resistance, R, decreases upon cooling (Figure 3b), indicating a typical metallic behavior. It is consistent with the band structure measured by angle-resolved photoemission spectroscopy (ARPES) where the Fermi level is located in the valence band (Figure S10, Supporting Information). As shown in Figure 3c, the magnitude of MR curves below T_C is ≈0.6% at 0.5 T, comparable with that of $CrTe_2$ thin flakes.[23] Notably, a sharp peak, corresponding to a large negative MR, appears at a low field when the temperature is close to T_C. With continuously increasing temperature, this peak becomes broad and a plateau appears, which is a signature of a magnetic phase transition.[33] It is in good agreement with the emergent AFM phase shown in previous magnetization measurements. The antiparallel alignment of the magnetization in the AFM phase produces an appreciable increase of the resistance, consistent with the phenomenon observed in spin valves.[1,2] In the plateau region with AFM ordering, electrons suffer a high scattering ratio and the conductivity is suppressed.[2,31] Increasing the field, the resistance drops sharply during the process from AFM phase to FM phase, among which the transmitting electrons with the same spin direction as $CrTe_2$ layers can pass freely. Further increasing the field, there is another slope change in the MR curves at high fields (for example, at 155 K and 0.28 T in Figure 3d, at 160 K and 0.38 T in Figure 3e), which is due to the saturation of magnetization.[34]

Consistent with pure $CrTe_2$ compound, the ground state of Cr_5Te_8 is FM,[24] whereas the self-intercalation gives rise to the AFM phase at elevated temperatures. Now we address the possible origins of this magnetic transition. The first mechanism that could lead to the observed AFM behavior is the formation of spin glass. In order to verify this possibility, frequency-dependent AC susceptibility was measured along c-axis (Figure S9, Supporting Information). The peak position of susceptibility curves (≈180 K) is independent of frequency, different from the frequency-dependent one found in spin glasses.[35] In addition, a helical AFM state could result in such a phenomenon as well.[36] The in-plane easy axis is usually a common feature of helical AFM states, contradictory to the observation of strong PMA in Cr_5Te_8. As a result, the potential of a helical AFM state could be ruled out. Another possible mechanism responsible for the AFM phase is the antiparallel interlayer coupling between adjacent $CrTe_2$ layers. Trace back to the source, the exchange interaction mechanisms of both intralayer and interlayer play a vital role in the magnetic ordering. AFM direct exchange interaction through t_{2g} orbitals and the FM Cr–Te–Cr superexchange interaction contribute to the magnetic coupling of intralayer. On the other hand, directional hybridization between Cr 3d-orbitals and Te 5p-orbitals gives rise to the interlayer superexchange coupling, which depends on the bond angles and bond distances of Cr–Te–Te–Cr path.[37] In addition, coupling through intercalated Cr is also worthy of consideration. According to previous reports, the lattice constant of $CrTe_2$ bulk along c-axis is 6.10 Å.[38] Strikingly, the vertical distance between $CrTe_2$ main layers dropped to 5.98 Å with interlayer Cr doping (Figure S2, Supporting Information). Notably, the distance between two nearest-neighbor Cr atoms plays an important role in determining the magnetic states. It has been theoretically predicted that the magnetic properties of $CrSiTe_3$ and $CrGeTe_3$ can be manipulated by modifying atomic distance under moderate strain.[39,40] Based on the

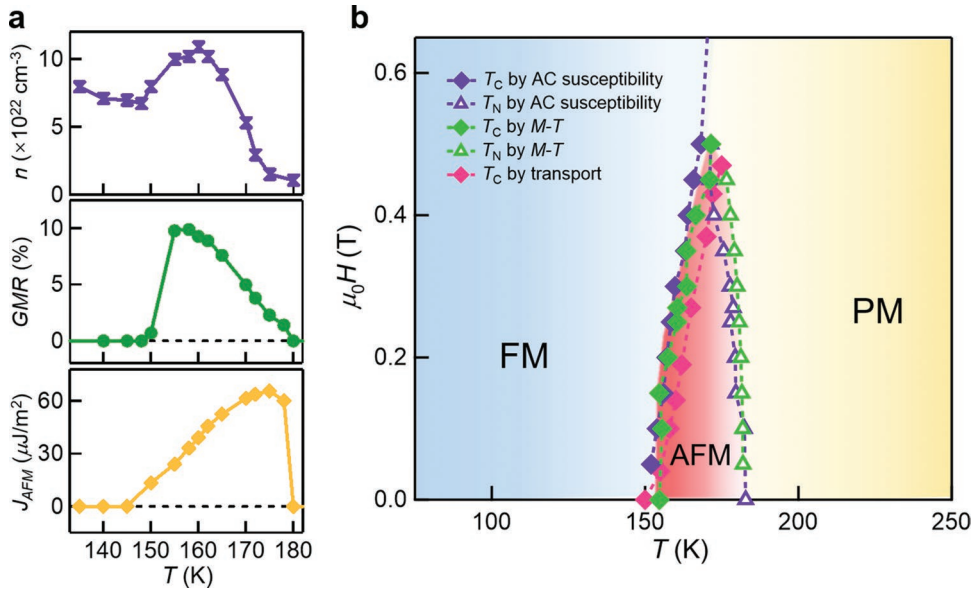

Figure 4. Temperature and magnetic field dependent magnetization reversal. a) Temperature dependence of the n, the GMR ratio and the J_{AFM}. b) Compiled magnetic field-temperature phase diagram. The green, purple, and pink symbols represent the critical points extracted from M–T curves, AC susceptibility, and electrical transport, respectively.

RKKY model, the interlayer magnetic coupling energy oscillates as a function of the nonmagnetic layer thickness in synthetic AFM multilayers.[7,41] Considering the temperature dependence of lattice constant included in Figure S13 (Supporting Information), the interlayer distance in a temperature window of 150–180 K may favor the antiparallel alignment among $CrTe_2$ main layers. Similarly, the oscillatory behavior of the interlayer exchange interaction versus the interlayer separation has also been revealed in the vdW $(Fe_{1-x}Co_x)_4GeTe_2$ magnets.[42] Besides, the variation of carrier density (n) can also be responsible for the AFM phase. The temperature dependence of n, GMR ratio and the AFM interlayer coupling strength (J_{AFM}) are summarized in **Figure 4**a. There is an apparent increase of n once entering the AFM phase, while it drops from the peak value of 1.09×10^{23} cm^{-3} at 160 K to 1.07×10^{22} cm^{-3} at the AFM phase boundary. In the itinerant Cr_5Te_8 system, the local spins and itinerant electrons are entangled with each other, which governs the spin dynamics.[43] The emergent AFM spin configuration is expected to also depend on the abrupt increase of n, while the exact exchange mechanism between conduction electrons and local spins remains to be investigated. Actually, the coupling between the magnetism and carriers is not limited to $CrTe_2$ compounds, but also applicable to magnetic topological insulators $Mn(Bi_{1-x}Sb_x)_4Te_7$ with magnetic phase transitions induced by a charge carrier engineering.[44]

A notable observation in Figure 4a is that, there is a rapid increase of the MR ratio once entering into the AFM state. With further increasing temperature, the GMR magnitude decreases and vanishes above the T_N, which presumably arises from two main contributions. The first one is the increased spin fluctuation at high temperature.[45,46] The other contribution comes from the reduced mean free path of electrons due to temperature dependent magnon scattering, phonon scattering and interfacial scattering. Despite GMR is related to the AFM coupling, J_{AFM} ($J_{AFM} = \mu_0 H_{ex} M_s t_{FM}$, where t_{FM} is the FM unit thickness and $\mu_0 H_{ex}$ represents the exchange field) shows an increasing trend with the increased temperature first, then reaches a peak of 66 μJ m^{-2} at 175 K, and finally reduces sharply near the T_N (Figure 4a), which is different from the temperature response of GMR ratio. J_{AFM} is governed by contributions from the spacer layers, magnetic layers and the interfaces. Near the T_C, the interlayer exchange coupling involves the transition from the FM mode to the AFM one at a higher temperature, resulting in an enhancement of J_{AFM}. With further increasing temperature, the softening of the Fermi edge, complex reflection coefficients at the interface as well as collective excitations within the magnetic layers make the coupling mechanism less effective.[47] The quantified J_{AFM} is one or two orders of magnitude lower than those of typical synthetic antiferromagnets composed of transition metals such as Fe/Cr (1.02×10^4 μJ m^{-2}), Co/Ru (4.83×10^3 μJ m^{-2}), and Co/Cu multilayers (2.21×10^3 μJ m^{-2}).[48] This weak J_{AFM} in Cr_5Te_8 resolves the conundrum of how to obtain changes in magnetic order with a moderate field, a behavior typically associated with weak magnetic interactions.

Based on the magnetization, susceptibility, and transport measurements, we plot the field-temperature phase diagram in Figure 4b. With the emergent AFM interlayer coupling, Cr_5Te_8 can be regarded as a magnetic-order competing system. Below T_C, main layers are ferromagnetically stacked along both interlayer and intralayer direction, resulting in a negligible MR. In the temperature range between T_C and T_N, the FM ordering within each $CrTe_2$ layer remains, while the interlayer coupling between adjacent $CrTe_2$ layers turns into AFM, bringing about the intrinsic GMR effect. A merger of T_C and T_N curves at high fields is clearly seen in the phase diagram, which is due to the enforced alignment of Cr magnetic moment by the Zeeman field.[49] Above T_N, the compound becomes paramagnetic and the MR vanishes. The presence of self-intercalation tunes the

interlayer magnetic coupling between $CrTe_2$ main layers, and thereby gives rise to the rich magnetic phase diagram. Apart from switching the interlayer coupling with an applied magnetic field, it is also possible to achieve analogous effects through varying temperature near the phase transition point.

3. Conclusion

In summary, we demonstrate an effective strategy to realize AFM interlayer exchange coupling through atomic-scale self-intercalation in crystal lattice. In particular, the antiparallel spins between adjacent $CrTe_2$ layers give rise to a pronounced GMR ratio and synthetic AFM phase in Cr_5Te_8 2D magnetic crystals, without requiring complex fabrication of multilayer structures. This technique could be extended to a broad class of 2D magnets to create potentially new mechanisms and properties. The experimental platform provides a hitherto unexplored but appealing approach to obtain the AFM interlayer exchange coupling, offering a new horizon in designing desired magnetic phases and engineering functional structures for 2D magnet-based spintronics.

4. Experimental Section

Growth of Cr_5Te_8 Single Crystals: High-quality Cr_5Te_8 single crystals were synthesized using self-flux method with high-purity elemental Cr (99.99%) and Te (99.999%) materials (from Alfa Aesar). A mixture of Cr and Te with an optimized molar ratio equivalent to 1:6 was sealed in evacuated quartz ampoules. Then it was heated up to 1050 °C and maintained for 1 day to allow sufficient homogenization, followed by slow cooling to 700 °C for a period of 1 week. Once the furnace reached 700 °C, the excess flux was removed from the crystals by centrifugation. It needs to be mentioned here that the growth method and parameters are different from those of $CrTe_2$[23] and $Cr_{1.2}Te_2$ single crystals[50] previously reported. The thicknesses of the Cr_5Te_8 bulk sample for magnetic and transport measurements is 0.692 mm. Cr_5Te_8 bulk can be well preserved in ambient conditions for at least one month as its pristine ones.

Structural and Magnetic Characterization: The crystal structure was examined by a high-resolution single crystal X-ray diffractometer (Bruker D8 Discover). The incident X-ray is from Cu-Kα emission and has a wave length of 1.5418 Å. The scan mode is θ–2θ. The magnetization and susceptibility measurements were performed using a Quantum Design superconducting quantum interference device (SQUID) magnetometer with a base temperature 2 K and magnetic field up to 7 T. The magneto-transport devices were confined to the Hall-bar geometry using the standard four-point probe method with room temperature cured silver paste as contacts. The MR measurements were performed on a Quantum Design Physical Property Measurement System (PPMS) with a base temperature 2 K and magnetic field up to 9 T.

X-Ray Absorption Spectroscopy and X-Ray Magnetic Circular Dichroism: XAS and XMCD measurements at the Cr $L_{2,3}$ absorption edges in total-electron yield (TEY) mode were performed at beamline I10 at Diamond Light Source, U.K. Oppositely circular polarized X-rays with 100% polarization were used to resolve XMCD signals in normal incidence. The light-helicity was switched in a magnetic field of 2 T, which was applied at 90° with respect to the film plane and in parallel with the incident beam. The dichroic spectrum was obtained by taking the difference of XAS spectra, i.e., $\sigma^+ - \sigma^-$.

Angle-Resolved Photoemission: After being cleaved in the load lock, the sample was transferred into the ARPES measurement chamber. ARPES measurements were performed with a SPECS PHOIBOS 150 hemisphere analyzer at 100 K with an energy resolution of 40 meV. A SPECS UVS 300 helium discharge lamp (He Iα = 21.2 eV) is used as the light source.

Supporting Information

Supporting Information is available from the Wiley Online Library or from the author.

Acknowledgements

X.Z., W.L., and W.N. contributed equally to this work. This work was supported by the National Key Research and Development Program of China (No. 2016YFA0300803, No. 2017YFA0206304), the National Basic Research Program of China (No. 2014CB921101), the National Natural Science Foundation of China (No. 61427812, 11774160, 11574137, 61474061, 61674079), Jiangsu Shuangchuang Program, the Natural Science Foundation of Jiangsu Province of China (No. BK20140054, BK20192006), UK EPSRC (EP/S010246/1), Leverhulme Trust (LTSRF1819\15\12), and Royal Society (IEC\NSFC\181680). X.Z. acknowledges the support of the fellowship of China Postdoctoral Science Foundation (2021M701590). G.B. was supported by the US National Science Foundation (NSF-DMR#1809160). Work of D.S. was supported by the U.S. Department of Energy, Basic Energy Sciences, Award Number DE-SC0019114. W.N. was supported by the Natural Science Foundation of China (Grant No. 11904174), Natural Science Foundation of Jiangsu Province (Grant No. BK20190729), NUPTSF (Grant No. NY220203). Diamond Light Source is acknowledged to I10 under proposal MM22532. The authors acknowledge the assistance of SUSTech Core Research Facilities.

Conflict of Interest

The authors declare no conflict of interest.

Data Availability Statement

The data that support the findings of this study are available from the corresponding author upon reasonable request.

Keywords

GMR effect, interlayer exchange coupling, self-intercalation, synthetic antiferromagnets, van der Waals magnets

Received: March 15, 2022
Revised: April 17, 2022
Published online: May 23, 2022

[1] M. N. Baibich, J. M. Broto, A. Fert, F. Nguyen Van Dau, F. Petroff, P. Etienne, G. Creuzet, A. Friederich, J. Chazelas, *Phys. Rev. Lett.* **1988**, *61*, 2472.
[2] G. Binasch, P. Grunberg, F. Saurenbach, W. Zinn, *Phys. Rev. B* **1989**, *39*, 4828.
[3] J. S. Moodera, L. R. Kinder, T. M. Wong, R. Meservey, *Phys. Rev. Lett.* **1995**, *74*, 3273.
[4] T. Song, X. Cai, W.-Y. M. Tu, X. Zhang, B. Huang, N. P. Wilson, K. L. Seyler, L. Zhu, T. Taniguchi, K. Watanabe, M. A. McGuire, D. H. Cobden, D. Xiao, W. Yao, X. Xu, *Science* **2018**, *360*, 1214.

[5] Q. Y. Jin, Y. B. Xu, H. R. Zhai, C. Hu, M. Lu, Q. S. Bie, Y. Zhai, G. L. Dunifer, R. Naik, M. Ahmad, *Phy. Rev. Lett.* **1994**, *72*, 768.
[6] D. M. Edwards, J. Mathon, R. B. Muniz, M. S. Phan, *Phys. Rev. Lett.* **1991**, *67*, 493.
[7] S. S. Parkin, N. More, K. P. Roche, *Phys. Rev. Lett.* **1990**, *64*, 2304.
[8] S. G. te Velthuis, J. S. Jiang, S. D. Bader, G. P. Felcher, *Phys. Rev. Lett.* **2002**, *89*, 127203.
[9] H. H. Kim, B. Yang, S. Li, S. Jiang, C. Jin, Z. Tao, G. Nichols, F. Sfigakis, S. Zhong, C. Li, S. Tian, D. G. Cory, G. X. Miao, J. Shan, K. F. Mak, H. Lei, K. Sun, L. Zhao, A. W. Tsen, *Proc. Natl. Acad. Sci. USA* **2019**, *116*, 11131.
[10] B. Huang, G. Clark, E. Navarro-Moratalla, D. R. Klein, R. Cheng, K. L. Seyler, D. Zhong, E. Schmidgall, M. A. McGuire, D. H. Cobden, W. Yao, D. Xiao, P. Jarillo-Herrero, X. Xu, *Nature* **2017**, *546*, 270.
[11] C. Gong, L. Li, Z. Li, H. Ji, A. Stern, Y. Xia, T. Cao, W. Bao, C. Wang, Y. Wang, Z. Q. Qiu, R. J. Cava, S. G. Louie, J. Xia, X. Zhang, *Nature* **2017**, *546*, 265.
[12] C. Gong, X. Zhang, *Science* **2019**, *363*, 706.
[13] W. Chen, Z. Sun, Z. Wang, L. Gu, X. Xu, S. Wu, C. Gao, *Science* **2019**, *366*, 983.
[14] S. Albarakati, C. Tan, Z.-J. Chen, J. G. Partridge, G. Zheng, L. Farrar, E. L. H. Mayes, M. R. Field, C. Lee, Y. Wang, Y. Xiong, M. Tian, F. Xiang, A. R. Hamilton, O. A. Tretiakov, D. Culcer, Y.u-J. Zhao, L. Wang, *Sci. Adv.* **2019**, *5*, eaaw0409.
[15] C. Hu, D. Zhang, F. Yan, Y. Li, Q. Lv, W. Zhu, Z. Wei, K. Chang, K. Wang, *Sci. Bull.* **2020**, *65*, 1072.
[16] S. Jiang, L. Li, Z. Wang, K. F. Mak, J. Shan, *Nat. Nanotechnol.* **2018**, *13*, 549.
[17] T. A. Tartaglia, J. N. Tang, J. L. Lado, F. Bahrami, M. Abramchuk, G. T. McCandless, M. C. Doyle, K. S. Burch, Y. Ran, J. Y. Chan, F. Tafti, *Sci. Adv.* **2020**, *6*, eabb9379.
[18] L. Meng, Z. Zhou, M. Xu, S. Yang, K. Si, L. Liu, X. Wang, H. Jiang, B. Li, P. Qin, P. Zhang, J. Wang, Z. Liu, P. Tang, Y. Ye, W. Zhou, L. Bao, H. J. Gao, Y. Gong, *Nat. Commun.* **2021**, *12*, 809.
[19] X. Zhang, Q. Lu, W. Liu, W. Niu, J. Sun, J. Cook, M. Vaninger, P. F. Miceli, D. J. Singh, S.-W. Lian, T.-R. Chang, X. He, J. Du, L. He, R. Zhang, G. Bian, Y. Xu, *Nat. Commun.* **2021**, *12*, 2492.
[20] Y. Wang, J. Yan, J. Li, S. Wang, M. Song, J. Song, Z. Li, K. Chen, Y. Qin, L. Ling, H. Du, L. Cao, X. Luo, Y. Xiong, Y. Sun, *Phys. Rev. B* **2019**, *100*, 024434.
[21] C. Chen, X. Chen, C. Wu, X. Wang, Y. Ping, X. Wei, X. Zhou, J. Lu, L. Zhu, J. Zhou, T. Zhai, J. Han, H. Xu, *Adv. Mater.* **2022**, *34*, 2107512.
[22] L.-Z. Zhang, X.-D. He, A.-L. Zhang, Q.-L. Xiao, W.-L. Lu, F. Chen, Z. Feng, S. Cao, J. Zhang, J.-Y. Ge, *APL Mater.* **2020**, *8*, 031101.
[23] X. Sun, W. Li, X. Wang, Q. Sui, T. Zhang, B. Wang, Z. Han, X. Han, Z. Zhang, *Nano Res.* **2020**, *13*, 3358.
[24] H. Y. Lv, W. J. Lu, D. F. Shao, Y. Liu, Y. P. Sun, *Phys. Rev. B* **2015**, *92*, 214419.
[25] C. T. Chen, Y. U. Idzerda, H. Lin, N. V. Smith, G. Meigs, E. Chaban, G. H. Ho, E. Pellegrin, F. Sette, *Phys. Rev. Lett.* **1995**, *75*, 152.
[26] W. Liu, D. West, L. He, Y. Xu, J. Liu, K. Wang, Y. Wang, *ACS Nano* **2015**, *9*, 10237.
[27] S. M. Thompson, *J. Phys. D: Appl. Phys.* **2008**, *41*, 093001.
[28] S. S. Parkin, *Phys. Rev. Lett.* **1993**, *71*, 1641.
[29] L. Jogschies, D. Klaas, R. Kruppe, J. Rittinger, P. Taptimthong, A. Wienecke, L. Rissing, M. C. Wurz, *Sensors-Basel* **2015**, *15*, 28665.
[30] S. S. P. Parkin, Z. G. Li, D. J. Smith, *Appl. Phys. Lett.* **1991**, *58*, 2710.
[31] J. Wu, F. Liu, M. Sasase, K. Ienaga, Y. Obata, R. Yukawa, K. Horiba, H. Kumigashira, S. Okuma, T. Inoshita, H. Hosono, *Sci. Adv.* **2019**, *5*, eaax9989.
[32] Y. Wang, C. Xian, J. Wang, B. Liu, L. Ling, L. Zhang, L. Cao, Z. Qu, Y. Xiong, *Phys. Rev. B* **2017**, *96*, 134428.
[33] D. Liang, J. P. DeGrave, M. J. Stolt, Y. Tokura, S. Jin, *Nat. Commun.* **2015**, *6*, 8217.
[34] Q. Wang, S. Sun, X. Zhang, F. Pang, H. Lei, *Phys. Rev. B* **2016**, *94*, 075135.
[35] K. Binder, A. P. Young, *Rev. Mod. Phys.* **1986**, *58*, 801.
[36] S. Kobayashi, *Phys. Rev. Lett.* **2011**, *106*, 057207.
[37] N. Sivadas, S. Okamoto, X. Xu, C. J. Fennie, D. Xiao, *Nano Lett.* **2018**, *18*, 7658.
[38] C. D. Freitas, R. Weht, A. Sulpice, G. Remenyi, P. Strobel, F. Gay, *J. Phys.: Condens. Matter* **2015**, *27*, 176002.
[39] N. Sivadas, M. W. Daniels, R. H. Swendsen, S. Okamoto, D. Xiao, *Phys. Rev. B* **2015**, *91*, 235425.
[40] X. Li, J. Yang, *J. Mater. Chem. C* **2014**, *2*, 7071.
[41] S. S. P. Parkin, *Annu. Rev. Mater. Sci.* **1995**, *25*, 357.
[42] J. Seo, E. S. An, T. Park, S. Y. Hwang, G. Y. Kim, K. Song, W. S. Noh, J. Y. Kim, G. S. Choi, M. Choi, E. Oh, K. Watanabe, T. Taniguchi, J. Park, Y. J. Jo, H. W. Yeom, S. Y. Choi, J. H. Shim, J. S. Kim, *Nat. Commun.* **2021**, *12*, 2844.
[43] I. A. Zaliznyak, Z. Xu, J. M. Tranquada, G. Gu, A. M. Tsvelik, M. B. Stone, *Phys. Rev. Lett.* **2011**, *107*, 216403.
[44] B. Chen, F. Fei, D. Wang, Z. Jiang, B. Zhang, J. Guo, H. Xie, Y. Zhang, M. Naveed, Y. Du, Z. Sun, H. Zhang, D. Shen, F. Song, *arXiv* **2020**, *2009*, 00039.
[45] R. Kienberger, E. Goulielmakis, M. Uiberacker, A. Baltuska, V. Yakovlev, F. Bammer, A. Scrinzi, T. Westerwalbesloh, U. Kleineberg, U. Heinzmann, M. Drescher, F. Krausz, *Nature* **2004**, *427*, 817.
[46] J. Ventura, J. P. Araujo, J. B. Sousa, A. Veloso, P. P. Freitas, *Phys. Rev. B* **2008**, *77*, 184404.
[47] S. Schwieger, W. Nolting, *Phys. Rev. B* **2004**, *69*, 224413.
[48] S. S. Parkin, *Phys. Rev. Lett.* **1991**, *67*, 3598.
[49] Q. L. He, X. Kou, A. J. Grutter, G. Yin, L. Pan, X. Che, Y. Liu, T. Nie, B. Zhang, S. M. Disseler, B. J. Kirby, W. Ratcliff Ii, Q. Shao, K. Murata, X. Zhu, G. Yu, Y. Fan, M. Montazeri, X. Han, J. A. Borchers, K. L. Wang, *Nat. Mater.* **2017**, *16*, 94.
[50] M. Huang, L. Gao, Y. Zhang, X. Lei, G. Hu, J. Xiang, H. Zeng, X. Fu, Z. Zhang, G. Chai, Y. Peng, Y. Lu, H. Du, G. Chen, J. Zang, B. Xiang, *Nano Lett.* **2021**, *21*, 4280.